Earth System
Dynamics

Regional dynamical and statistical downscaling temperature, humidity and wind speed for the Beijing region under stratospheric aerosol injection geoengineering

Jun Wang[1], **John C. Moore**[1,2], **Liyun Zhao**[1], **Chao Yue**[1], and **Zhenhua Di**[3]

[1]College of Global Change and Earth Systems Science, Beijing Normal University, 100875 Beijing, China
[2]Arctic Centre, University of Lapland, Rovaniemi, Finland
[3]State Key Laboratory of Earth Surface Processes and Resource Ecology, Faculty of Geographical Science, Beijing Normal University, 100875 Beijing, China

Correspondence: Liyun Zhao (zhaoliyun@bnu.edu.cn) and John C. Moore (john.moore.bnu@gmail.com)

Abstract. We use four Earth system models (ESMs) to simulate climate under the modest greenhouse emissions RCP4.5 (Representative Concentration Pathway), the "business-as-usual" RCP8.5 and the stratospheric aerosol injection G4 geoengineering scenarios. These drive a 10 km resolution dynamically downscaled model (Weather Research and Forecasting, WRF) and a statistically bias-corrected (Inter-Sectoral Impact Model Intercomparison Project, ISIMIP) and downscaled simulation in a 450×330 km domain containing the Beijing Province, ranging from 2000 m elevation to sea level. The 1980s simulations of surface temperatures, humidities and wind speeds using statistical bias correction make for a better estimate of mean climate determined by ERA5 reanalysis data than does the WRF simulation. However correcting the WRF output with quantile delta mapping bias correction removes the offsets in mean state and results in WRF better reproducing observations over 2007–2017 than ISIMIP bias correction. The WRF simulations consistently show 0.5 °C higher mean annual temperatures than from ISIMIP due both to the better resolved city centres and also to warmer winter temperatures. In the 2060s WRF produces consistently larger spatial ranges of surface temperatures, humidities and wind speeds than ISIMIP downscaling across the Beijing Province for all three future scenarios. The WRF and ISIMIP methods produce very similar spatial patterns of temperature with G4 and are always cooler than RCP4.5 and RCP8.5, by a slightly larger amount with ISIMIP than WRF. Humidity scenario differences vary greatly between ESMs, and hence ISIMIP downscaling, while for WRF the results are far more consistent across ESMs and show only small changes between scenarios. Mean wind speeds show similarly small changes over the domain, although G4 is significantly windier under WRF than either RCP scenario.

1 Introduction

The global-mean surface air temperature has increased by 0.9–1.2 °C relative to 1850–1900 (Eyring et al., 2021), with a rapid rise during the 2010s. Extreme climate events are becoming more frequent (Pachauri et al., 2014), impacting human health and mortality rates (Pielke et al., 2013). Earth system models (ESMs), despite being global in extent, can-

not simulate phenomena smaller than their spatial resolution (typically 1–2 °) with the same fidelity as higher-resolution models with much smaller domains. Higher-resolution models include regional climate models and the Weather Research and Forecasting model (WRF) which are generally driven by ESMs at their lateral boundaries. WRF has been widely used as a dynamical downscaling method for future climate projection at small and regional scales (Bao et al.,

2015; Brewer and Mass, 2016; Kong et al., 2019). Kong et al. (2019) found that WRF was satisfactory in reproducing spatiotemporal distribution and trends of extreme climate indices for China.

Geoengineering via increasing planetary albedo as a method of avoiding the worst excesses of climate heating has been actively discussed in climate research for well over a decade (Shepherd, 2009). The most widely studied albedo modification type (e.g. Lenton et al., 2009; Robock et al., 2009) is via stratospheric aerosol injection (SAI). To standardise and aid the evaluation of SAI in ESM simulations, Kravitz et al. (2011) proposed the Geoengineering Model Intercomparison Project (GeoMIP), with Phase 1 including two different SAI scenarios using sulfates as the aerosol and with greenhouse gas emissions from the Representative Concentration Pathway (RCP) 4.5 scenario. The impacts of SAI on temperature (Schmidt et al., 2012), precipitation (Tilmes et al., 2013) and the cryosphere (Moore et al., 2019) have been widely studied. They found that the global mean temperatures are indeed reduced but along with some regional inequalities, such as relative over-cooling of the tropics and under-cooling of the polar regions. The impacts on precipitation are relatively modest, especially compared with the less mitigated greenhouse gas scenarios. Several studies have considered global-scale impacts on temperature and precipitation extremes under both SAI and other geoengineering types designed to enhance planetary albedo (Curry et al., 2014; Aswathy et al., 2015; Ji et al., 2018), and some studies have focused on regional impacts such as in Europe (Jones et al., 2018), East Asia (Kim et al., 2020) or the Maritime Continent (Kuswanto et al., 2021).

Statistical downscaling has often been used as an alternative to dynamical methods, avoiding the significant computing resources needed to run models such as WRF. Statistical downscaling is based on the relationships found historically between ESM output and observed climate variables and is very widely used in regional impact studies (Wilby et al., 2004). All models produce results with a bias from observations, and future simulations require either bias correction or results to be shown as climate anomalies relative to some control scenario. The Inter-Sectoral Impact Model Intercomparison Project (ISIMIP, https://www.isimip.org/, last access: 11 November 2022) consortium has produced methods (Hempel et al., 2013) widely used to correct the bias from CMIP5 (Climate Model Intercomparison Project phase 5) and GeoMIP outputs (McSweeney et al., 2016; Moore et al., 2019; Kuswanto et al., 2021). In our paper, we compare ISIMIP statistical downscaling methods and output from WRF dynamical downscaling and assess their performance for simulating the climate condition in the provinces around Beijing under SAI.

The greater Beijing region lies in complex terrain, surrounded by hills and mountains on three sides, with a flat plain to the southeast coast (Fig. 1). We explore the effect of geoengineering on surface temperature, wind and humidity

in this domain. We nest a 10 km resolution domain inside a much larger 30 km resolution domain, driven at the boundaries with ESM output. We use the WRF model to dynamically downscale three time slices: 1979–1989, 2007–2017 and 2059–2069, driven by four ESMs simulating the historical, RCP 4.5, RCP8.5 and the GeoMIP G4 scenarios (Table 1). The 10 km resolution we use is not designed to study urban processes. Instead, we examine differences in downscaling at resolutions higher than, but comparable with, statistical downscaling methods that are likely to continue to be used in most geoengineering studies globally. To the best of our knowledge, this paper is the first to make dynamic downscaling of geoengineering scenarios.

We firstly show the differences between statistical downscaling with bias correction and dynamical downscaling without bias correction in the 1979–1989 period. This will show that a statistical downscaled and bias-corrected result, by design, has closer agreement with observations, despite its absence of physics, than the dynamically downscaled simulation. For the recent past period 2007–2017 we use the quantile delta mapping method to statistically correct the bias of the WRF simulation and assess its performance. Finally, we show the projections in the future period 2059–2069 for the greater Beijing region where global temperature differences under different greenhouse gas and G4 scenarios are known to be large. The paper is organised as follows: Sect. 2 describes the WRF model setup and parameterisation, statistical downscaling and bias-correction methods. The results from the historical simulation and future projections on the surface temperature, humidity, and wind speed are all given in Sect. 3. Finally, a summary of the main findings and the conclusion is given in Sect. 4.

2 Data and method

2.1 ESMs and scenarios (data description)

We focus on exploring the effect of SAI on surface meteorological conditions (temperature, humidity and wind) over the domain using four different dynamically and statistically downscaled ESMs. In the simulations, we use three different scenarios: RCP4.5 and RCP8.5 and the GeoMIP G4 scenario. RCP4.5 is a scenario that never exceeds a radiative forcing of $4.5 \, \mathrm{W \, m^{-2}}$ (Thomson et al., 2011), while RCP8.5 is an unmitigated emissions scenario leading to a radiative forcing of $8.5 \, \mathrm{W \, m^{-2}}$ at the end of the 21st century (Riahi et al., 2011). The GeoMIP experiment G4 specifies injection of sulfur dioxide into the equatorial lower stratosphere at a rate of $5 \, \mathrm{Mt \, yr^{-1}}$ from 2020 to 2069 (Kravitz et al., 2011). These scenarios span a useful range of climate scenarios: RCP4.5 is similar (Vandyck et al., 2016) to the expected trajectory of emissions under the 2015 Paris climate accord Nationally Determined Contributions (NDCs); RCP8.5 represents a formerly business-as-usual scenario that still provides a large signal-to-noise ratio "worst case" scenario; G4 represents
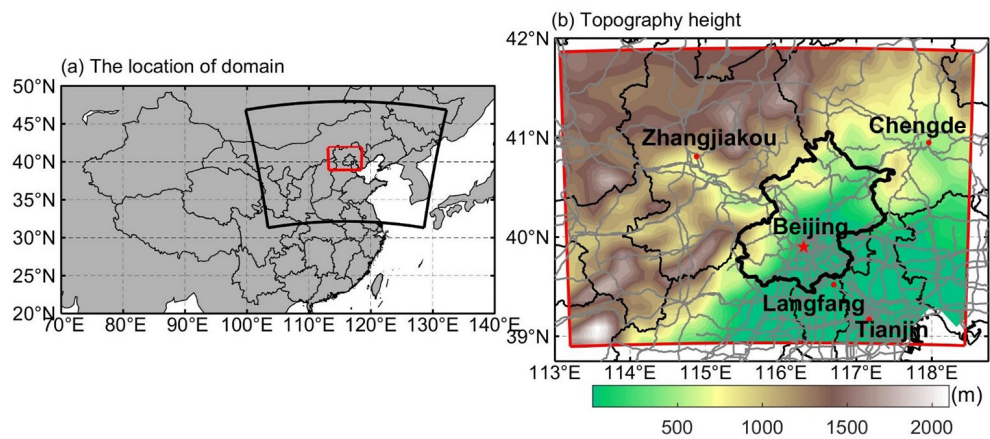
Figure 1. (a) Map of East Asia with Chinese provincial boundaries marked in black. The 10 km WRF domain (red box) is nested inside the 30 km resolution domain (large black sector), which is centred on 116° E, 40° N on a Lambert projection. **(b)** The topography and primary roads (grey curves) of the 10 km resolution domain from panel **(a)**. The provincial boundaries are marked in black with the heavier line demarking the Beijing region. The major metropolitan centres of Beijing, Tianjin, Chengde and Langfang are marked in red.

Table 1. The simulations in our study.

Periods	Scenarios	Goal of the simulation
1979–1989	Historical	Compare ISIMIP statistical downscaling and bias correction with WRF
2007–2017	RCP4.5	Assess the performance of ISIMIP and WRF with bias correction
2059–2069	RCP4.5, RCP8.5, G4	Future downscaled climates by ISIMIP and WRF with bias correction

a similar radiative forcing as a quarter of the 1991 Mount Pinatubo volcanic eruption every year. If SAI were ever done then it would certainly use a much more sophisticated injection procedure than G4, perhaps designed to maintain hemispheric temperature balance and preserve pole–Equator temperature gradients (Macmartin and Kravitz, 2016). However, G4 levels of SAI are within the linear response of temperature reduction to material injected and within a range of radiative forcing that might be plausible or reasonable to consider (Niemeier and Timmreck, 2015). GeoMIP has also developed new experiments for use with CMIP6 level ESMs (Kravitz et al., 2015).

ESM data required as input data for WRF include meteorological fields, land surface and soil properties: specific humidity, air temperature, eastward wind, northward wind, near surface air pressure and the elevations of 30 pressure levels from 1000 to 30 hPa, soil temperatures, humidities and water contents, and sea level pressures. Only four ESMs can meet the data requirements (Table 2). We only use one single realisation (r1i1p1 using the CMIP5 nomenclature) for each model since all downscaling runs are extremely computationally expensive and some of the models have only a single realisation available.

Here we use ERA5 reanalysis data as our reference. This fifth-generation ECMWF atmospheric reanalysis of global climate combining a huge number of historical observations into global estimates by advanced modelling and data assim-

Table 2. ESMs used in this study.

Model	Resolution (long × lat)	Reference
BNU-ESM	128 × 64	Ji et al. (2014)
HadGEM2-ES	192 × 144	Collins et al. (2011)
MIROC-ESM	128 × 64	Watanabe et al. (2011)
MIROC-CHEM-ESM	128 × 64	Watanabe et al. (2011)

ilation systems (Hersbach et al., 2020) has been widely used for meteorological data analysis (Chen et al., 2021; Huo et al., 2022; Lee et al., 2022; Zhang et al., 2022). The performance of ERA5 for temperature (Gong et al., 2022), relative humidity (Zhang et al., 2021) and wind speed (Yu et al., 2019) analysed over China suggests it well reproduces the observed meteorological data in climatology and interannual variations. We also use the 31 km resolution ERA5 6 h reanalysis data during 1 January 1979–31 December 1989 to correct ESM climate fields at the domain boundaries as required by WRF (Hersbach et al., 2018). ERA5 reanalysis near-surface meteorological elements (2 m temperature, 2 m humidity and 10 m wind speed) are significantly correlated with observations over the area (Meng et al., 2018). We use daily temperature, humidity and wind from ERA5 for the period 1980–1989 and 2008–2017 to statistically bias cor-

rect the ESMs variables and assess the performance of WRF downscaling.

2.2   WRF

The WRF model adopts a compressible non-hydrostatic equilibrium equation and a variety of physical parameterisation schemes and data assimilation which can realise high-resolution weather forecasts at various scales (Michalakes et al., 2001). Xu et al. (2012) used WRF to improve the bias in global climate model simulations of extreme weather events. WRF needs 6 h input data, which do not exist for most variables in the ESMs climate simulation output. So, we use the available monthly ESM data to estimate 6 h input data with a pseudo global warming downscaling method (PGW-DS, Kawase et al., 2009) using ERA5 data bilinearly interpolated to the same grid as the ESM output:

$$M_f = R_h - \overline{M}_h + \overline{M}_f, \tag{1}$$

where M_f is the ESM-driven WRF model 6 h input data and R_h is 6 h data from ERA5 reanalysis during the historical period 1979–1989. For the period 1979–1989, $\overline{M}_h$ is the monthly data of ERA5 and $\overline{M}_f$ is the monthly data of ESMs under the historical scenario. For the period 2007–2017, $\overline{M}_h$ is the monthly data of ESMs during 1979–1989 under the historical scenario, and $\overline{M}_f$ takes the monthly data of ESMs during 2007–2017 under RCP4.5. For the period 2059–2069, $\overline{M}_h$ is the monthly data of ESMs during 1979–1989 under historical scenario and $\overline{M}_f$ takes the monthly data of ESMs during 2059–2069 under RCP4.5, RCP8.5 and G4 scenarios.

This study uses WRF version 3.9.1 with two nested domains, where the inner domain (longitude × latitude: 45×33) has a resolution of 10 km and the outer domain (80×58) has a resolution of 30 km (Fig. 1). The model has 30 vertical layers from the surface to 50 hPa. The integration time step is 3 min. We set the parameterisations following a study on the numerical simulation of urbanisation on regional climate in China (Wang et al., 2012) as follows: the WRF Single Moment 6-class (WSM6, Hong et al. 2006), the new version of the rapid radiative transfer model (RRTMG, Iacono et al., 2008) for both the long-wave and short-wave radiation, the MM5 similarity surface layer scheme (Paulson et al., 1970), the Yonsei University (YSU) planetary boundary layer (PBL) scheme (Noh et al., 2003), the Kain–Fritsch scheme for atmospheric convection (Kain, 2004), and the Noah land surface model (Chen and Dudhia, 2001).

Putting the ESMs data as initial and boundary conditions into the WRF Preprocessing System (WPS; Fig. 2) is challenging. We downloaded all the required monthly data (see Table S1) from four ESMs in the three periods (1979–1989, 2007–2017, 2059–2069) and 6 h historical data from ERA5 (1979–1989). Then, we used the PGW method to get the 6 h input data during three periods (see Eq. 1). We then used Climate Data Operators (CDOs) to convert the input data in NC format files into GRIB format files that WPS can recognise.

In all three simulated periods, the initial year is considered as spin-up time and is not included in our analysis.

2.3   ISIMIP statistical downscaling and bias correction

This method corrects daily variability on the premise that the monthly trend of the modelled variable is unchanged (Hempel et al., 2013). Here, we take the data from one grid point and for some single months as an example to illustrate the procedure. It includes three steps.

In step 1, we firstly bilinearly interpolate the model data to the same grid points of reanalysis data before bias correction.

In step 2, monthly bias-corrected data are found by a multi-year averaged difference between the model output and reanalysis data in our referenced period:

$$M_m^* = \overline{R_m} - \overline{M_m} + M_m. \tag{2}$$

The M_m^* is the bias-corrected monthly data; $\overline{R_m}$ and $\overline{M_m}$ are the multi-year averaged values in this month from reanalysis data and model data during the reference period, respectively. M_m is the modelled monthly data. The subscript m represents monthly. In this step, ISIMIP does not correct the daily variability of modelled data.

In step 3, we correct the modelled daily variability to a linear regression residual:

$$\Delta M_d^* = \bar{B} \times (M_d - M_m). \tag{3}$$

The ΔM_d^* is the bias-corrected residual daily data from model. M_d is the modelled daily data. The subscript d represents daily. $(M_d - M_m)$ represents the modelled daily residual values in this month, and the residual of reanalysis data can be obtained in the same way. $\bar{B}$ is the linear regression coefficient of daily residual values between reanalysis data and model data during our referenced period. Then, we can get the bias-corrected modelled daily data:

$$M_d^* = M_m^* + \Delta M_d^*. \tag{4}$$

The M_d^* is the bias-corrected daily data of model. Therefore, ISIMIP corrects the monthly mean and its daily variability. Here, we use the ERA5 reanalysis data as reanalysis data in our study. For convenience we use the term ISIMIP-ESM to denote the output from the ESMs after applying the ISIMIP statistical downscaling and bias-correction methodology.

2.4   Quantile mapping (QM) and quantile delta mapping (QDM)

Quantile mapping has been widely used as a statistical bias-correction and downscaling method (Li and Babovic, 2019; Kuswanto et al., 2021), and annual and monthly biases of all variables can be reduced to nearly zero (Wilcke et al., 2013). As a bias-correction method, quantile mapping can reproduce the frequency of different types of extreme heat wave
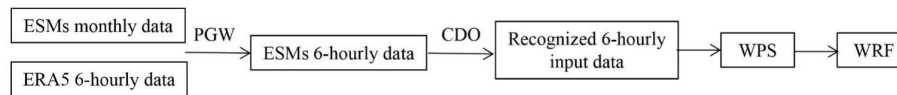
Figure 2. The WRF flow chart. PGW refers to the pseudo global warming downscaling method, and CDOs refer to Climate Data Operators used for generating the WRF recognisable "GRIB" format input data. WPS is the WRF Preprocessing System.

events well (Schoof et al., 2019). Here we use the empirical cumulative distribution function (CDF) to correct the biases:

$$M_d^* = F_R^{-1}(F_H(M_d)), \tag{5}$$

where M_d^* is the daily data after bias correction, F is the cumulative distribution function (CDF), F^{-1} is the inverse, subscript R represents the ERA5 reanalysis data, subscript H represents historical simulation results and M_d is daily model output in the historical simulations. This method keeps the model and observational data CDFs as consistent as possible.

QDM is similar to QM but is non-stationary. It considers the time variability between the historical simulation and future projection; hence it is preferable for our task here (Salvi et al., 2011):

$$M_d^* = F_R^{-1}(F_F(M_d)) + \left(M_d - F_H^{-1}(F_F(M_d))\right). \tag{6}$$

The M_d^* and M_d are bias-corrected and raw daily model outputs in the future simulations. The subscript R represents the ERA5 reanalysis data; the subscripts F and H represent model outputs from future and historical simulations, respectively. To preserve the spatial information of the high-resolution WRF model result, we do bias correction on daily value averaged in the whole inner domain (Fig. 1b) rather than separately for each grid point.

For the WRF simulations during 2007–2017 and 2059–2069, we use the QDM method to correct biases. Similar to ISIMIP-ESM, we use the terms WRF-ESM and WRF-QDM-ESM to represent results of WRF driven by the ESM and WRF driven by ESM after QDM bias correction, respectively.

3 Results

3.1 Historical simulation: WRF and ISIMIP downscaling comparison

We compare the simulations of mean temperature, relative humidity and wind speed from raw ESM output downscaled to ERA5 resolution, ISIMIP-ESM and WRF-ESM in Beijing during the 1980s in Fig. 3. Figure 3a shows the annually averaged 2 m ERA5 temperatures in Beijing, with a mean of 7 °C and highs in the southeast (12 °C) and lows in the northwest, which correlates with the topography (Fig. 1). Relative humidity (Fig. 3e) varies between 50 %–55 %, with the city centre a little drier than the suburbs. Similarly, wind speed is

low in the city centre with highs in the higher north western hills and south eastern plain (Fig. 3i).

The temperatures from the raw ESM outputs in Beijing have less range than both ISIMIP-ESM and WRF-ESM results due to their coarser resolution and obvious bias. The mean temperatures of MIROC-ESM and MIROC-ESM-CHEM over the domain are about 8 °C, while HadGEM2-ES and BNU-ESM are cooler, and all ESM have a large cold bias compared with ERA5 (Fig. S1). ISIMIP-ESM forces the model mean data to agree with ERA5 mean observations by design and also downscales the ESM data to the observational resolution (Fig. 3c, g, k). The resulting ISIMIP-ESM means are indistinguishable by eye from the ERA5 mean in Fig. 3, though the ESM trends over time are preserved and the seasonality and other measures of variability are ESM-dependent and differ from ERA5.

WRF has a finer resolution than ERA5 and clearly shows higher temperatures in the centre of Beijing with cool temperatures over the mountains. WRF temperatures driven by MIROC-ESM and MIROC-ESM-CHEM are higher in the Beijing and Tianjin city centres than ERA5, ISIMIP-MIROC and ISIMIP-MIROC-CHEM outputs, while the temperatures in the suburbs are a little lower than from ERA5 and ISIMIP-ESM. Temperatures from HadGEM2-ES-driven WRF are a little colder than that of ERA5 and ISIMIP-HadGEM2 over Beijing (Fig. S1). WRF also produces lower relative humidity in the centre of Beijing and higher humidity in the north and west of city, consistent with the pattern of temperatures. Humidity under WRF tends to be lower in the urban centre (45 %) and higher in the suburban areas (60 %) than ISIMIP and ERA5. Relative humidities of all ESMs are higher than ERA5 (Fig. S2). The humidities of WRF under different ESMs are noticeably different from each other, although MIROC-ESM and MIROC-ESM-CHEM are similar (Fig. S2). Wind speeds in all ESMs are greater than ERA5, except HadGEM2-ES (Fig. S3). ISIMIP reduces all ESMs to essentially the ERA5 pattern as with temperature and humidity. WRF winds for all four ESMs are greatly overestimated. All WRF simulations have spatial patterns very different from ERA5, with maximums associated with the northern and western higher ground.
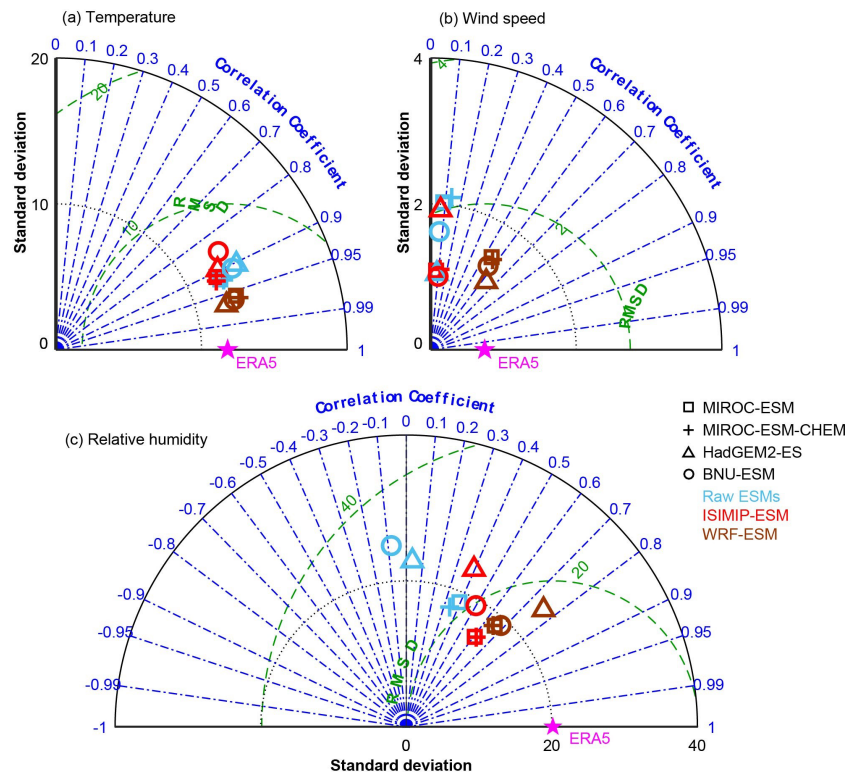
The temperature, relative humidity and wind speed distributions (Fig. 4) illustrate bias and across-ESM differences for the WRF simulations. Both MIROC-ESM and MIROC-ESM-CHEM overestimate the probability of high temperatures. ISIMIP-HadGEM2 overestimates the likelihood of high temperatures when compared with ERA5, while
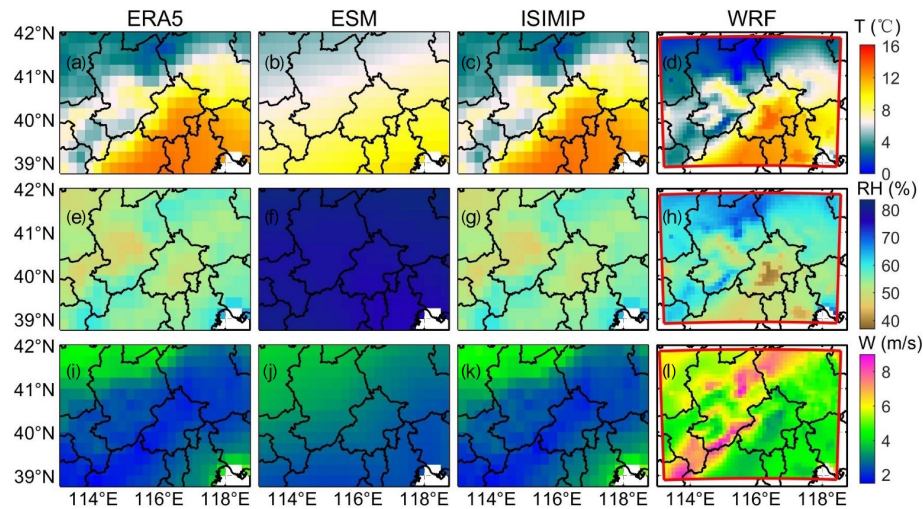
Figure 3. The region containing the high-resolution WRF domain (red boundary in right column maps), with city boundaries marked in black. The spatial distribution of mean 2 m temperature **(a–d)**, relative humidity **(e–h)** and 10 m wind speed **(i–l)** from ERA5, downscaled ESM ensemble mean before any bias correction, ISIMIP-ESM ensemble mean and the WRF-ESM ensemble mean in the high-resolution domain (Fig. 1) during 1980–1989. The results for the four ESMs are shown separately in Figs. S1–S3 in the Supplement along with the bias-corrected versions.
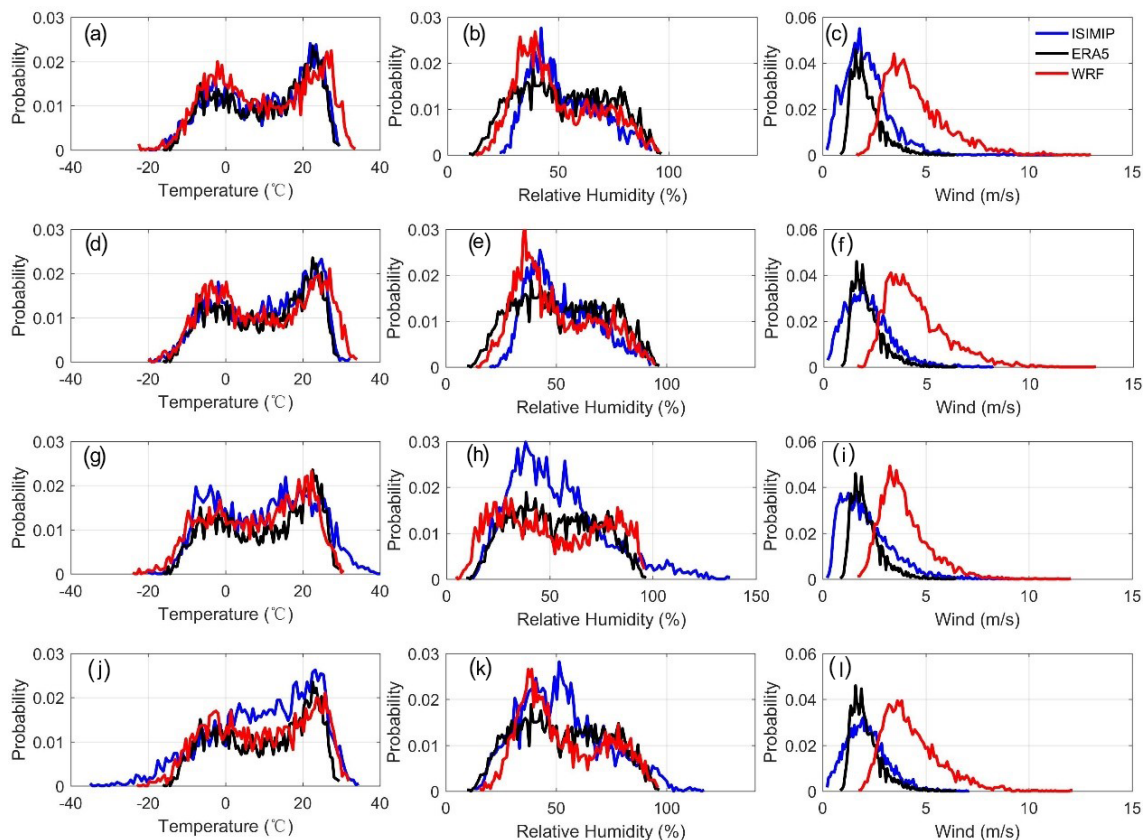
Figure 4. The probability density function (pdf) for daily mean temperature, relative humidity and wind speed for MIROC-ESM **(a–c)**, MIROC-ESM-CHEM **(d–f)**, HadGEM2-ES **(g–i)** and BNU-ESM **(j–l)** under WRF (red lines) and ISIMIP statistical bias-correction method (blue lines) in the Beijing province (Fig. 1) during 1980–1989. The black line is ERA5 reanalysis data. Values of humidity exceeding 100 % can occur with ISIMIP downscaling.

Figure 5. Taylor diagram for daily temperature **(a)**, wind speed **(b)** and relative humidity **(c)** of four ESMs using two downscaling methods, i.e. ISIMIP (red) and WRF (brown) compared to ERA5 data during 1980–1989 in Beijing. The blue symbols are the data from raw ESMs. The skill of downscaling methods is reflected by the distance from each symbol to the point labelled "ERA5", the ERA5 reanalysis data. The blue lines are the correlation coefficient which represents the similarity between each downscaling data and reanalysis data. The green contours are root mean standard deviation (RMSD), and black contours are standard deviation.

ISIMIP-BNU overestimates both high and low temperature extremes. WRF performs well for all four ESMs compared with ISIMIP, which produces unphysical relative humidities exceeding 100 % for HadGEM2-ES and BNU-ESM. ISIMIP winds for all four ESMs tend to increase the frequency of low winds and winds exceeding $5 \, \text{m s}^{-1}$. WRF winds are close to twice that of ERA5. Overall, results after ISIMIP show closer mean values to ERA5, while the pdf's for WRF are closer to ERA5, but the differences between ISIMIP and WRF are small except for wind speed.

Figure 5 shows the Taylor diagrams (Taylor, 2001), which can be used to assess the skill of two downscaling methods applied to meteorological data. Temperatures from raw MIROC-ESM and MIROC-ESM-CHEM output show better performance than the other two models. WRF has a better correlation coefficient (>0.95) than ISIMIP and smaller RMSD for all four ESMs. Wind speed of all four ESM outputs have correlation coefficients <0.1 with ERA5. ISIMIP greatly reduces errors and variance (except for HadGEM2-ES) but does not improve correlation. WRF has better correlation, has lower errors and shows better skill on simulating wind speed than ISIMIP, despite its systematic bias in magnitude.

3.2   Bias correction for WRF

We use QDM to correct biases of the WRF results for the 2008–2017 historical simulation. The temperature, relative humidity and wind speed from ERA5 over Beijing during 2008–2017 (Fig. 6) have a very similar pattern with those during the 1980s (Fig. 3). Average temperatures slightly increased over Beijing when compared with the 1980s. Average humidities in most places during 2008–2017 are slightly higher than during the 1980s, while in the northwest of Zhangjiakou, where temperatures rose fastest, humidity shows a slight decrease (Figs. 3 and 6). Winds in Beijing between these 2 decades did not change.

WRF-QDM-ESM simulations of the three variables (Fig. 6) exhibit geographic patterns that are the same as those during the 1980s (Fig. 3). QDM bias correction makes the temperature hotter and the humidity drier especially in high mountains and cities, producing spatial patterns closer to ERA5 (Fig. 6). QDM bias correction greatly improves wind speed results from uncorrected values of $4–5 \, \text{m s}^{-1}$ to $1.5–2.5 \, \text{m s}^{-1}$ across most areas. The mean 2 m temperature of WRF-QDM-HadGEM is hotter than the other three ESMs ($16 \, °\text{C}$ in the centre of Beijing), while the other three reach only $14 \, °\text{C}$, which is close to ERA5 (Fig. S4e–h). WRF-
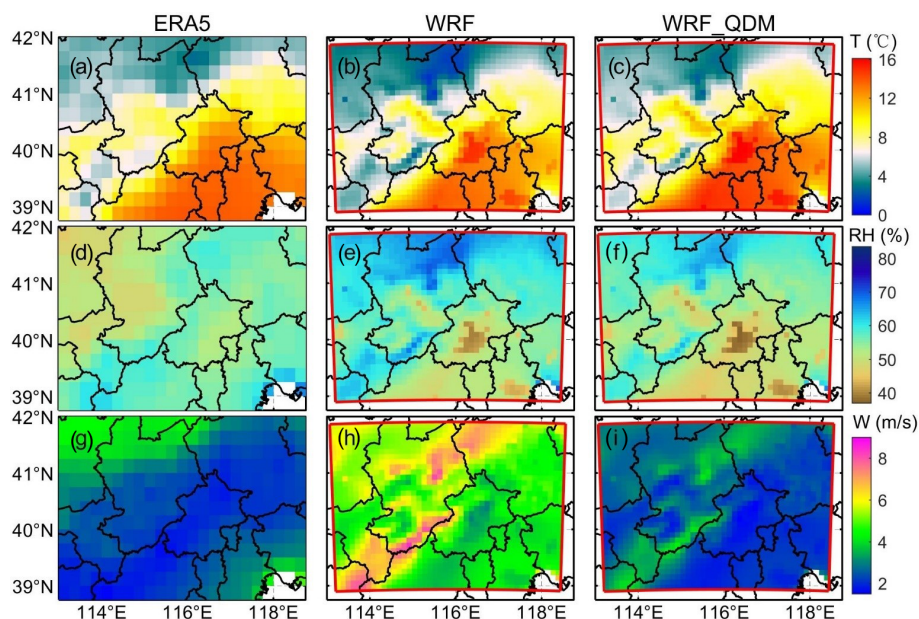
Figure 6. The spatial distribution of mean 2 m temperature **(a–c)**, relative humidity **(d–f)** and 10 m wind speed **(g–i)** from ERA5, WRF-ESM and WRF-QDM-ESM ensemble mean during 2008–2017. Figures S4–S6 show the four ESM results separately.
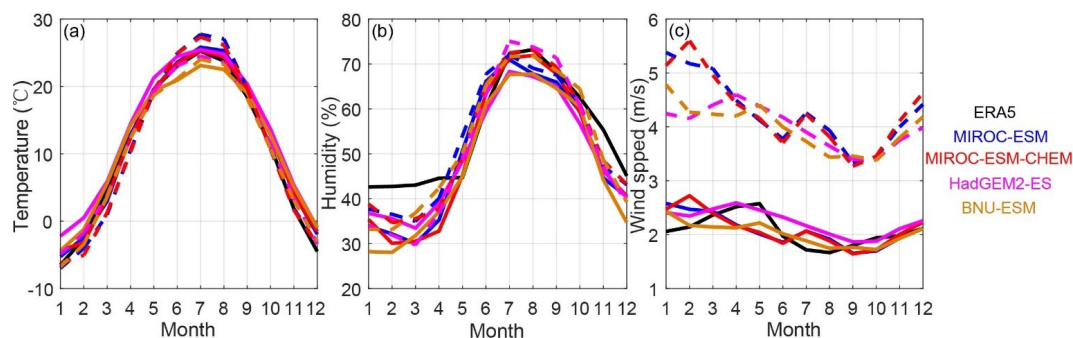
Figure 7. Seasonal cycle of multi-year averaged monthly temperature **(a)**, relative humidity **(b)** and wind speed **(c)** during 2008–2017 for Beijing. The solid lines are the WRF-QDM-ESM results, and the dashed lines are the WRF-ESM results.

QDM-MIROC and WRF-QDM-MIROC-CHEM are more humid than WRF-QDM-HadGEM2 and WRF-QDM-BNU. The wind speed of WRF-QDM-BNU is a little slower than other three ESMs.

The seasonal cycle of average daily temperature simulated by WRF is close to ERA5 (Fig. 7). However, the temperature of WRF-QDM-BNU shows a colder bias than the raw results in the summer, and the temperature of WRF-QDM-HadGEM2 shows a warmer bias than the results from WRF-HadGEM2 in the winter. For humidity, the overall performance of WRF-QDM-ESM is not good, and they all show a dry bias relative to ERA5 from July to the following May. After bias correction, the wind speeds from all ESMs clearly decrease to the same range as ERA5. Winds from HadGEM2-ES show the best agreement in both the quantity and seasonality with ERA5, but QDM does not change the seasonality of wind speed, just its amplitude.

The skill of QDM for correcting daily temperature, relative humidity and wind from the biased WRF-ESM are shown in Fig. 8. QDM changes the errors but has little effect on the correlation with the ERA5 data. While temperature and wind speed all improve with QDM, humidities from WRF-QDM-ESM have a lower performance than does the corresponding WRF-ESM results except for WRF-QDM-HadGEM2. We regard bias correcting as necessary for WRF outputs.

3.3 Future projections

We now look at temperature, humidity and wind projections for 2060–2069. Figure 9 shows maps of ensemble mean 2 m temperature (Fig. 9a–f), relative humidity (Fig. 9g–l) and 10 m wind speed (Fig. 9m–r) under the G4, RCP4.5
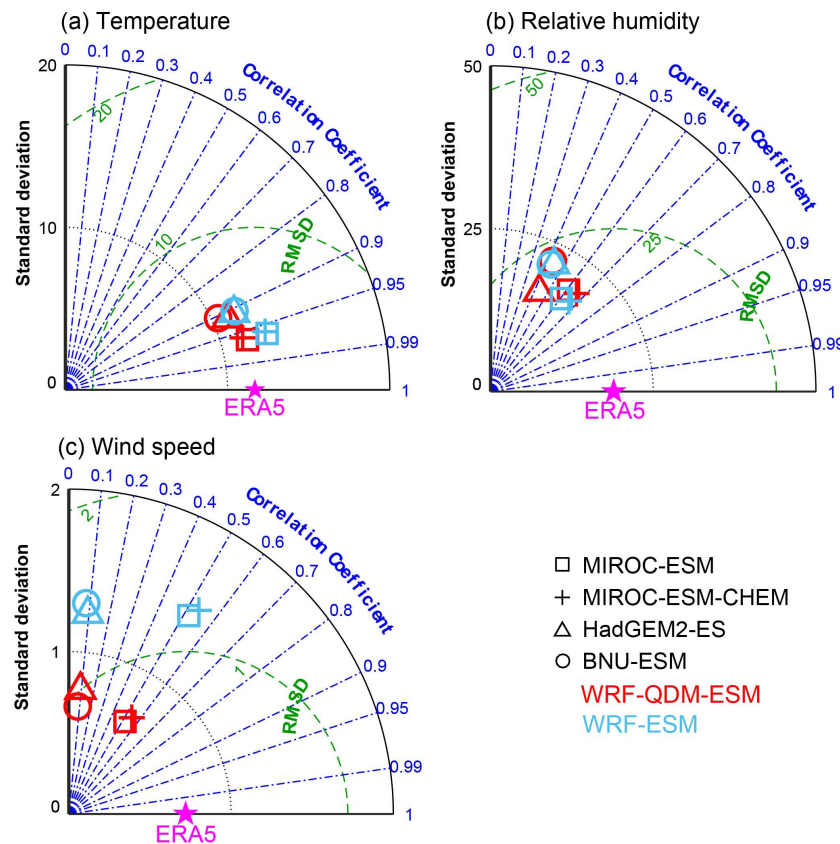
Figure 8. Taylor diagram for daily temperature **(a)**, relative humidity **(b)** and wind speed **(c)** of WRF driven by four ESMs results with QDM bias correction (red) and without bias correction (blue) compared to ERA5 reanalysis data (purple star) during 2008–2017 in Beijing.

and RCP8.5 scenarios. Mean temperatures over the domain are 12.5, 13.3 and 14.8 °C from ISIMIP-ESM and 13.1, 13.8 and 15.2 °C from WRF-QDM-ESM under G4, RCP4.5 and RCP8.5 scenarios, respectively. The higher city centre temperatures from WRF-QDM-ESM account for the 0.5 °C difference from ISIMIP-ESM. Both ISIMIP-ESM and WRF-QDM-ESM produce similar overall temperature patterns driven by topography. Relative humidities under geo-engineering and RCP scenarios are almost the same. Mean model relative humidities are 53.8 %, 53.6 % and 53.4 % by ISIMIP-ESM, and slightly wetter than 50.0 %, 49.7 % and 50.2 % from WRF-QDM-ESM, under G4, RCP4.5 and RCP8.5 scenarios respectively. This is mainly due to lower humidities with WRF-QDM-ESM in city centres. Wind spatial patterns are clearly different from ISIMIP-ESM and WRF-QDM-ESM. The wind speed in the southwest of the domain from ISIMIP-ESM is low, while WRF-QDM-ESM winds are lowest in the city centre. Although there are some differences in details between different ESMs, the overall results are similar to those of ensemble means (Figs. S7–S12).

Figure 10 shows temperature, humidity and wind anomalies from WRF-QDM-ESM and ISIMIP-ESM simulations. The mean temperature in the 2060s under G4 is 1–2 °C higher than that during 2008–2017. Temperatures from both

ISIMIP-ESM and WRF-QDM-ESM are cooler over the whole domain under G4 than those under RCP4.5 by 0.1–1.5 °C, while there is a larger cooling effect of 1.6–2.8 °C under G4 relative to RCP8.5 (Table 3). There is large across-model spread with the two MIROC models having smaller differences (G4-RCP4.5) than the other two models (Table 3), and the two MIROC models show larger differences from each other with ISIMIP-ESM than with WRF-QDM-ESM. Relative humidity anomalies exhibit large differences under different scenarios for ISIMIP-ESM and WRF-QDM-ESM. G4 humidity from ISIMIP-ESM shows a slight reduction of 1 percentage point relative to the 2010s over Beijing, while there is an increment of similar magnitude from the WRF-QDM-ESM results. When compared to RCP4.5 scenario, the humidity under G4 from ISIMIP-ESM shows a slight (1 percentage point) increase, but that from WRF-QDM-ESM shows no statistically significant change. The differences of relative humidities from WRF-QDM-ESM and ISIMIP-ESM between G4 and RCP8.5 show opposite trends, although differences are slight. ISIMIP-ESM winds under G4 are a little slower than those during the 2010s and show no significant difference between G4 and RCP4.5. Compared to RCP8.5, G4 winds from ISIMIP-ESM increase by 0.15 m s^{-1} mainly in the south of the domain. Winds from
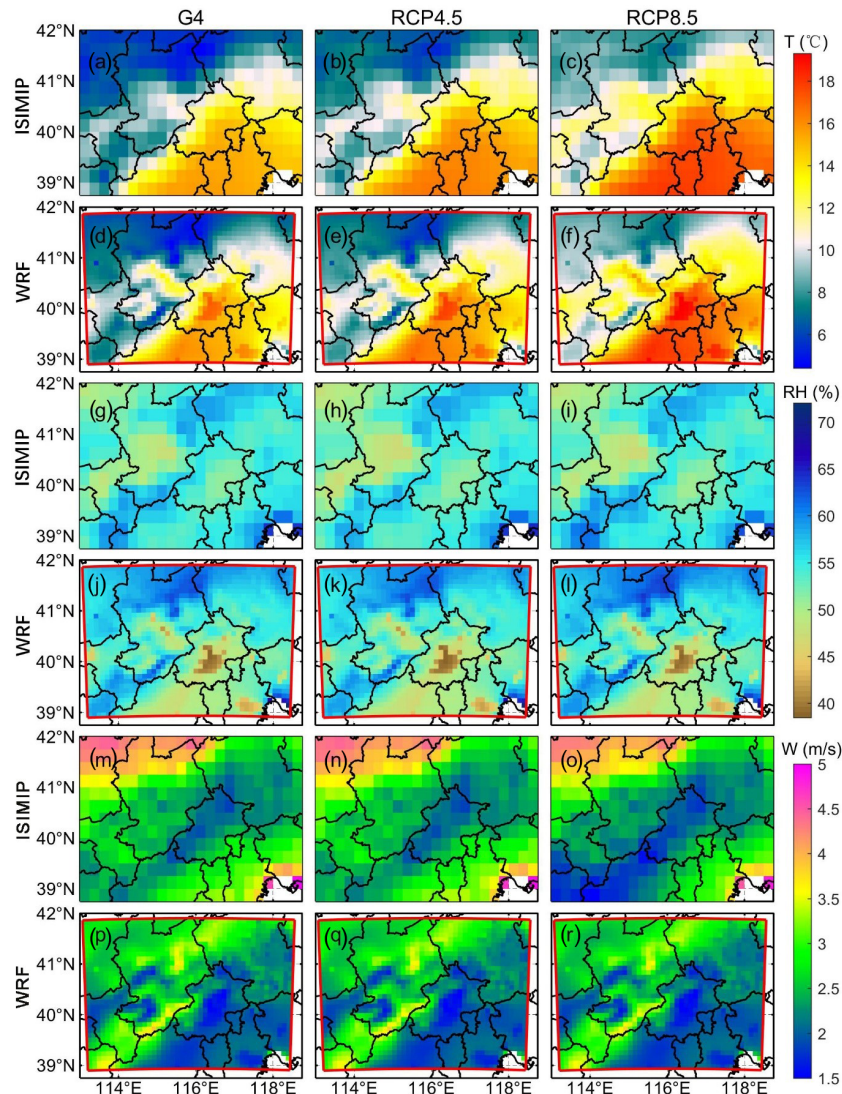
Figure 9. The spatial distribution of ensemble mean 2 m temperature **(a–f)**, relative humidity **(g–l)** and 10 m wind speed **(m–r)** under G4, RCP4.5 and RCP8.5 scenarios based on ISIMIP-ESM and WRF-QDM-ESM results during 2060–2069.

WRF-QDM-ESM show very small changes with slight increases relative to the RCP scenarios. Humidity anomalies from ISIMIP have a difference under G4 relative to RCP8.5 in the southwest of the domain, where wind speed anomalies show an obvious positive change, while for WRF there are no particular patterns.

4   Discussion and conclusions

We have explored the impact of geoengineering on surface temperature, humidity and wind speed over Beijing during 2060–2069 using statistical bias correction and dynamical downscaling. We evaluated the performance of ISIMIP and WRF methods during 1980–1989 based on the historical simulations from four ESMs. WRF output needs to be bias

corrected for it to be comparable with observations or statistically downscaled and bias-corrected output. We use the QDM method to correct the bias in the WRF results since QDM ensures that the pdf of simulation results is consistent with the reanalysis data. Because we want to keep the high spatial resolution of the WRF model simulation, we do not correct biases grid cell by grid cell, which would produce output at the reanalysis resolution, but instead do bias correction for daily mean temperature, humidity and wind speed over the domain.

The raw output from the ESMs of temperature, humidity and wind speed have no clear spatial distribution over the domain because cities occupy only a few ESM grid cells. Statistical bias correction and downscaling by the ISIMIP method produces output at the same resolution as the observational reanalysis data and matches its spatial distribution.

Table 3. Difference of 2 m temperature between G4 and ERA5 in the 2010s and RCP scenarios in the 2060s for the high-resolution domain (Fig. 1). Bold indicates the differences or changes are significant at the 95 % confidence level according to the Wilcoxon signed rank test (units: °C).

	G4-2010s		G4-RCP4.5		G4-RCP8.5	
	ISIMIP	WRF	ISIMIP	WRF	ISIMIP	WRF
MIROC-ESM	**1.9**	**2.0**	**−0.9**	**−0.4**	**−2.3**	**−1.9**
MIROC-ESM-CHEM	**2.4**	**2.0**	−0.1	−0.4	**−1.6**	**−1.7**
HadGEM2-ES	**1.0**	**0.8**	**−1.4**	**−1.5**	**−2.8**	**−2.7**
BNU-ESM	**1.1**	**1.0**	**−1.2**	**−0.7**	**−2.6**	**−2.2**
Ensemble	**1.6**	**1.5**	**−0.9**	**−0.7**	**−2.3**	**−2.2**
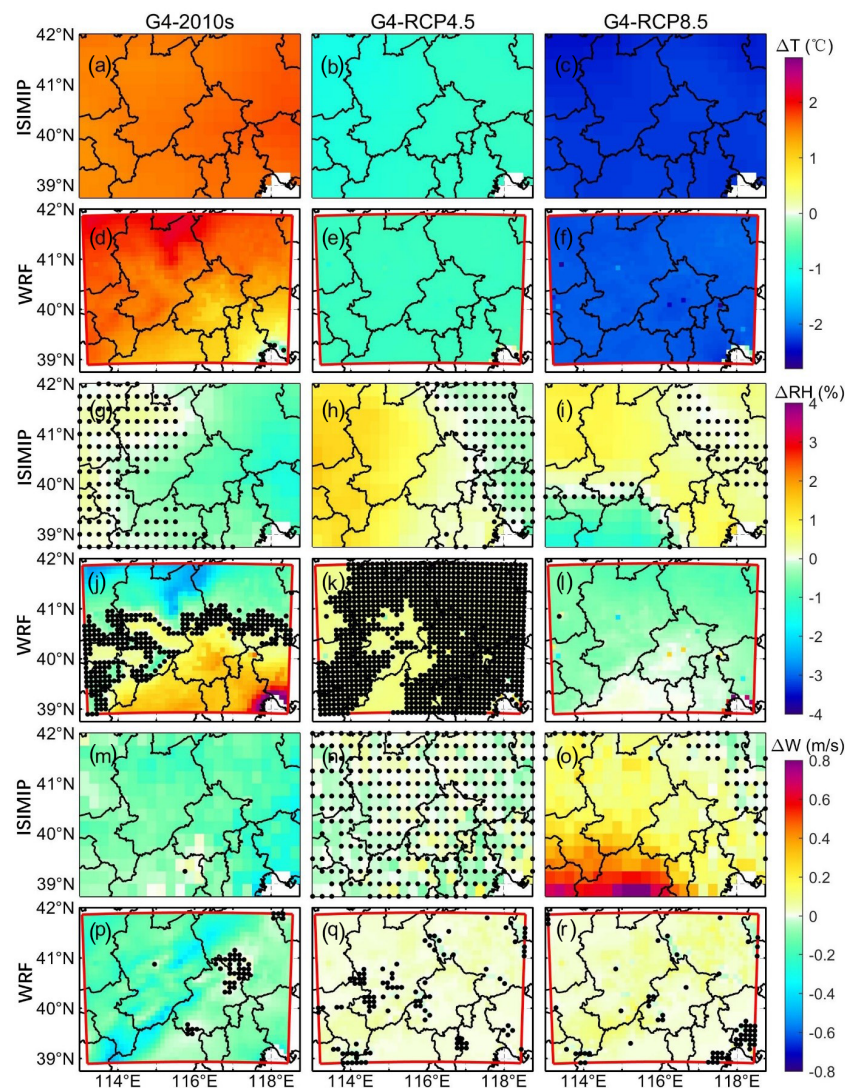
Figure 10. Spatial pattern of ensemble mean 2 m temperature **(a–f)**, relative humidity **(g–l)** and 10 m wind **(m–r)** scenario differences: G4-2010s (left column), G4-RCP4.5 (middle column) and G4-RCP8.5 (right column) based on ISIMIP-ESM and WRF-QDM-ESM results. 2010s means the results simulated during 2008–2017, and G4, RCP4.5 and RCP8.5 mean the results projected during 2060–2069. Stippling indicates grid points where differences are not significant at the 95 % confidence level according to the Wilcoxon signed rank test. Figures S13–S18 show the results for each ISIMIP-ESM and WRF-QDM-ESM separately.

The ISIMIP method is designed to preserve trends and the long-term mean value the same as the observations (Hempel et al., 2013). Dynamically downscaling demands a higher-resolution grid, and WRF produces an output at a spatial resolution independent of the resolution of the reanalysis data. The WRF results not only produce characteristics consistent with the reanalysis data, but also depict the more detailed meteorological characteristics created by the complex underlying land surface that are input to WRF. The WRF simulation during 1980–1989 showed higher temperatures in the city centres than those in the suburbs and lower temperatures in the western and northern mountainous areas. This pattern is created by the joint actions of latitude, terrain and underlying surface. The pattern of relative humidity distribution is anticorrelated to temperature, with lower humidity in the urban centre, while humidities in some mountainous areas are higher. This is similar to the pattern of humidity from 42 AWSs (automatic weather stations) in Beijing during 2007–2015 (Yang et al., 2017) and due mainly to the underlying surface and the transpiration of the urban area being less than that of the suburbs (Dou et al., 2020). Wind speeds inside the Beijing urban area are low but reach a maximum in its western foothills. Urbanisation increases surface roughness, lowering wind speed (Liu et al., 2020). Correlation coefficients of wind speed between the WRF downscaling results and ERA5 for all four ESM raw results are all <0.1. Zha et al. (2020) and Jiang et al. (2017) also found similar low correlations. Zha et al. (2020) project the near-surface wind speed over eastern China based on a CMIP5 dataset and found that 18 of the 24 ESMs analysed show negative correlations with observed wind speed during 1979–2005. The low correlations are to be expected when considering variability in simulated weather at high temporal resolution. Jiang et al. (2017) found that differences in CMIP5 model wind responses to the East Asian monsoon in China are related to model parameterisation and horizontal resolution. The pdf of temperature suggests that the WRF result is more realistic and closer to observations than results from ISIMIP, although the MIROC-ESM and MIROC-ESM-CHEM show a higher probability for high temperatures. The pdf of humidity strongly indicates that WRF performs better than ISIMIP. But WRF tends to overestimate the wind speed even though the shape of pdf is more similar to observations than that of ISIMIP output. Many studies show that WRF frequently overestimates wind speed, e.g. in the Gulf of Mexico (Lee et al., 2011), in the coastal cities of Spain (Chen et al., 2012) and in south eastern Texas (Ngan et al., 2013), because of imperfect surface representation (e.g. urban vegetation and surface morphology). Overestimated surface wind speed in WRF is caused by using smoothed topography in the model (Jimenez and Dudhia, 2012). Overall, for temperature and humidity, the results of WRF are better than those of ISIMIP, and both are better than the original ESM output. WRF has better correlation with observations than ISIMIP.

Applying QDM bias correction to WRF reduces model and monthly dependent differences. Temperatures, both before and after bias correction, have high correlations with ERA5, and QDM makes little difference. WRF relative humidity, however, is always drier than that of ERA5 in winter whether revised or not. Wind speeds are lowered after bias correction to the same levels as ERA5, but QDM does not have a clear effect on correlation (Zhao et al., 2017).

The spatial distribution of temperature, humidity and wind speed are roughly similar in all three periods assessed, that is the 1980s, 2010s and 2060s, whether from ISIMIP-ESM or WRF-QDM-ESM. Our analysis shows that mean temperature under G4 is always lower than that under RCP4.5 and RCP8.5. Although it does not return temperatures to the historical level, that was not the design of the experiments, which instead simply explore the effects of injecting roughly $\frac{1}{4}$ the amount of SO_2 into the equatorial lower stratosphere as the 1991 Mount Pinatubo eruption every year for 50 years. Using ISIMIP downscaling leads to larger differences between scenarios than using WRF. HadGEM2-ES shows the largest difference in temperatures between G4 and RCP scenarios of the four ESMs we studied. For the relative humidity, ISIMIP-ESM and WRF-QDM-ESM give opposite (but small) signed anomalies between G4 and RCP4.5 in our domain.

This paper is the first to use WRF for regional dynamic downscaling of geoengineered climates and impacts on relatively small spatial and temporal scales, which can be useful for regions that need higher resolutions than ERA5, and statistical downscaling can supply. The differences between statistical downscaling and dynamic downscaling in the Beijing region, that extends from sea level to mountains about 2000 m in elevation, may appear rather modest. But even these modest differences in derived temperatures and humidities can make for large differences in compound indices such as apparent temperature, particularly when assessing future risk to urban populations.

Author contributions. JCM and LZ designed the experiments, and JW performed the simulations. JW and JCM prepared the article with contributions from all co-authors.

References

Aswathy, V. N., Boucher, O., Quaas, M., Niemeier, U., Muri, H., Mülmenstädt, J., and Quaas, J.: Climate extremes in multi-model simulations of stratospheric aerosol and marine cloud brightening climate engineering, Atmos. Chem. Phys., 15, 9593–9610, https://doi.org/10.5194/acp-15-9593-2015, 2015.

Bao, J., Feng, J., and Wang, Y.: Dynamical downscaling simulation and future projection of precipitation over China, J. Geophys. Res.-Atmos., 120, 8227–8243, https://doi.org/10.1002/2015JD023275, 2015.

Brewer, M. C. and Mass, C. F.: Projected Changes in Heat Extremes and Associated Synoptic- and Mesoscale Conditions over the Northwest United States, J. Climate, 29, 6383–6400, https://doi.org/10.1175/JCLI-D-15-0641.1, 2016.

Chen, B., Stein, A. F., Castell, N., de la Rosa, J. D., de la Campa, A. M., S., Gonzalez-Castanedo, Y., and Draxler, R. R.: Modeling and surface observations of arsenic dispersion from a large Cu-smelter in southwestern Europe, Atmos. Environ., 49, 114–122, https://doi.org/10.1016/j.atmosenv.2011.12.014, 2012.

Chen, F. and Dudhia, J.: Coupling an Advanced Land Surface–Hydrology Model with the Penn State–NCAR MM5 Modeling System, Part I: Model Implementation and Sensitivity, Mon. Weather Rev., 129, 569–585, https://doi.org/10.1175/1520-0493(2001)129<0569:CAALSH>2.0.CO;2, 2001.

Chen, S., Cao, R., Xie, Y., Zhang, Y., Tan, W., Chen, H., Guo, P., and Zhao, P.: Study of the seasonal variation in Aeolus wind product performance over China using ERA5 and radiosonde data, Atmos. Chem. Phys., 21, 11489–11504, https://doi.org/10.5194/acp-21-11489-2021, 2021.

Collins, W. J., Bellouin, N., Doutriaux-Boucher, M., Gedney, N., Halloran, P., Hinton, T., Hughes, J., Jones, C. D., Joshi, M., Liddicoat, S., Martin, G., O'Connor, F., Rae, J., Senior, C., Sitch, S., Totterdell, I., Wiltshire, A., and Woodward, S.: Development and evaluation of an Earth-System model – HadGEM2, Geosci. Model Dev., 4, 1051–1075, https://doi.org/10.5194/gmd-4-1051-2011, 2011.

Curry, C. L., Sillmann, J., Bronaugh, D., Alterskjaer, K., Cole, J. N. S., Ji, D., Kravitz, B., Kristjánsson, J. E., Moore, J. C., Muri, H., Niemeier, U., Robock, A., Tilmes, S., and Yang, S.: A multi-model examination of climate extremes in an idealized geoengineering experiment, J. Geophys. Res.-Atmos., 119, 3900–3923, https://doi.org/10.1002/2013JD020648, 2014.

Dou, J., Bornstein, R., Miao, S., and Zhang, Y.: Observation and Simulation of a Bifurcating Thunderstorm over Beijing, J. Appl. Meteorol. Climatol., 59, 2129–2148, https://doi.org/10.1175/JAMC-D-20-0056.1, 2020.

Eyring, V., Gillett, N. P., Achuta Rao, K. M., Barimalala, R., Barimalala Parrillo, M., Bellouin, N., Cassou, C., Durack, P. J., Kosaka, Y., McGregor, S., Min, S., Morgenstern, O., Ying, S. Human Influence on the Climate System. In Climate Change 2021: The Physical Science Basis, Contribution of Working Group I to the Sixth Assessment Report of the Intergovernmental Panel on Climate Change, 2nd ed., edited by: Masson-Delmotte, V., Zhai, P., Pirani, A., Connors, S. L., Péan, C., Berger, S., Caud, N., Chen, Y., Goldfarb, L., Gomis, M. I., Huang, M., Leitzell, K., Lonnoy, E., Matthews, J. B. R., Maycock, T. K., Waterfield, T., Yelekçi, O., Yu, R. and Zhou, B., Cambridge University Press, UK, In Press, 2021.

Gong, Y., Yang, S., Yin, J., Wang, S., Pan, X., Li, D., and Yi, X.: Validation of the Reproducibility of Warm-Season Northeast China Cold Vortices for ERA5 and MERRA-2 Reanalysis, J. Appl. Meteorol. Clim., 61, 1349–1366, https://doi.org/10.1175/JAMC-D-22-0052.1, 2022.

Hempel, S., Frieler, K., Warszawski, L., Schewe, J., and Piontek, F.: A trend-preserving bias correction – the ISI-MIP approach, Earth Syst. Dynam., 4, 219–236, https://doi.org/10.5194/esd-4-219-2013, 2013.

Hersbach, H., Bell, B., Berrisford, P., Biavati, G., Horányi, A., Muñoz Sabater, J., Nicolas, J., Peubey, C., Radu, R., Rozum, I., Schepers, D., Simmons, A., Soci, C., Dee, D., and Thépaut, J-N.: ERA5 hourly data on pressure levels from 1979 to present, Copernicus Climate Change Service (C3S) Climate Data Store (CDS), cds [data set], https://doi.org/10.24381/cds.bd0915c6, 2018.

Hersbach, H., Bell, B., Berrisford, P., Hirahara, S., Horányi, A., Muñoz-Sabater, J., Nicolas, J., Peubey, C., Radu, R., Schepers, D., Simmons, A., Soci, C., Abdalla, S., Abellan, X., Balsamo, G., Bechtold, P., Biavati, G., Bidlot, J., Bonavita, M., Chiara, G., Dahlgren, P., Dee, D., Diamantakis, M., Dragani, R., Flemming, J., Forbes, R., Fuentes, M., Geer, A., Haimberger, L., Healy, S., Hogan, R., Hólm, E., Janisková, M., Keeley, S., Laloyaux, P., Lopez, P., Lupu, C., Radnoti, G., Rosnay, P., Rozum, I., Vamborg, F., Villaume, S., and Thépaut, J.: The

ERA5 global reanalysis, Q. J. Roy. Meteorol. Soc., 146, 1999–2049, https://doi.org/10.1002/qj.3803, 2020.

Hong, S. Y. and Lim, J. O. J.: The WRF single-moment 6-class microphysics scheme (WSM6), J. Korean Meteor. Soc., 42, 129–151, 2006.

Huo, L., Wang, J., Jin, D., Luo, J., Shen, H., Zhang, X., Min, J., and Xiao, Y.: Increased summer electric power demand in Beijing driven by preceding spring tropical North Atlantic warming, Atmos. Ocean. Sci. Lett., 15, 100146, https://doi.org/10.1016/j.aosl.2021.100146, 2022.

Iacono, M. J., Delamere, J. S., Mlawer, E. J., Shephard, M. W., Clough, S. A., and Collins, W. D.: Radiative forcing by long-lived greenhouse gases: Calculations with the AER radiative transfer models, J. Geophys. Res.-Atmos., 113, D13, https://doi.org/10.1029/2008JD009944, 2008.

Ji, D., Wang, L., Feng, J., Wu, Q., Cheng, H., Zhang, Q., Yang, J., Dong, W., Dai, Y., Gong, D., Zhang, R.-H., Wang, X., Liu, J., Moore, J. C., Chen, D., and Zhou, M.: Description and basic evaluation of Beijing Normal University Earth System Model (BNU-ESM) version 1, Geosci. Model Dev., 7, 2039–2064, https://doi.org/10.5194/gmd-7-2039-2014, 2014.

Ji, D., Fang, S., Curry, C. L., Kashimura, H., Watanabe, S., Cole, J. N. S., Lenton, A., Muri, H., Kravitz, B., and Moore, J. C.: Extreme temperature and precipitation response to solar dimming and stratospheric aerosol geoengineering, Atmos. Chem. Phys., 18, 10133–10156, https://doi.org/10.5194/acp-18-10133-2018, 2018.

Jiang, Y., Xu, X., Liu, H., Dong, X., Wang, W., and Jia, G.: The underestimated magnitude and decline trend in near-surface wind over China, Atmos. Sci. Lett., 18, 475–483, 2017.

Jimenez, P. and Dudhia, J.: Improving the representation of resolved and unresolved topographic effects on surface wind in the WRF model, J. Appl. Meteorol. Climatol., 51, 300–316, 2012.

Jones, A. C., Hawcroft, M. K., Haywood, J. M., Jones, A., Guo, X., and Moore, J. C.: Regional climate impacts of stabilizing global warming at 1.5 K using solar geoengineering, Earth. Fut., 6, 230–251, https://doi.org/10.1002/2017EF000720, 2018.

Kain, J. S.: The Kain-Fritsch convective parameterization: an update, J. Appl. Meteorol., 43, 170–181, https://doi.org/10.1175/1520-0450(2004)043<0170:TKCPAU>2.0.CO;2, 2004.

Kawase, H., Yoshikane, T., Hara, M., Kimura, F., Yasunari, T., Ailikun, B., Ueda, H., and Inoue, T.: Intermodel variability of future changes in the Baiu rainband estimated by the pseudo global warming downscaling method, J. Geophys. Res.-Atmos., 114, D24, https://doi.org/10.1029/2009JD011803, 2009.

Kim, D. H., Shin, H. J., and Chung, I. U.: Geoengineering: Impact of marine cloud brightening control on the extreme temperature change over East Asia, Atmosphere, 11, 1345, https://doi.org/10.3390/atmos11121345, 2020.

Kong, X., Wang, A., Bi, X., and Wang, D.: Assessment of temperature extremes in China using RegCM4 and WRF, Advan. Atmos. Sci., 36, 363–377, https://doi.org/10.1007/s00376-018-8144-0, 2019.

Kravitz, B., Robock, A., Boucher, O., Schmidt, H., Taylor, K. E., Stenchikov, G., and Schulz, M.: The geoengineering model intercomparison project (GeoMIP), Atmos. Sci. Lett., 12, 162–167, https://doi.org/10.1002/asl.316, 2011.

Kravitz, B., Robock, A., Tilmes, S., Boucher, O., English, J. M., Irvine, P. J., Jones, A., Lawrence, M. G., MacCracken, M., Muri, H., Moore, J. C., Niemeier, U., Phipps, S. J., Sillmann, J., Storelvmo, T., Wang, H., and Watanabe, S.: The Geoengineering Model Intercomparison Project Phase 6 (GeoMIP6): simulation design and preliminary results, Geosci. Model Dev., 8, 3379–3392, https://doi.org/10.5194/gmd-8-3379-2015, 2015.

Kuswanto, H., Kravitz, B., Miftahurrohmah, B., Fauzi, F., Sopahaluwaken, A., and Moore, J. C.: Impact of solar geoengineering on temperatures over the Indonesian Maritime Continent, Int. J. Climatol., 42, 2795–2814, https://doi.org/10.1002/joc.7391, 2021.

Lee, S., Lung, S., Chiu, P., Wang, W., Tsai, I., and Lin, T.: Northern Hemisphere Urban Heat Stress and Associated Labor Hour Hazard from ERA5 Reanalysis, Int. J. Environ. Res. Public Health, 19, 8163, https://doi.org/10.3390/ijerph19138163, 2022.

Lee, S.-H., Kim, S.-W., Angevine, W. M., Bianco, L., McKeen, S. A., Senff, C. J., Trainer, M., Tucker, S. C., and Zamora, R. J.: Evaluation of urban surface parameterizations in the WRF model using measurements during the Texas Air Quality Study 2006 field campaign, Atmos. Chem. Phys., 11, 2127–2143, https://doi.org/10.5194/acp-11-2127-2011, 2011.

Lenton, T. M. and Vaughan, N. E.: The radiative forcing potential of different climate geoengineering options, Atmos. Chem. Phys., 9, 5539–5561, https://doi.org/10.5194/acp-9-5539-2009, 2009.

Li, X. and Babovic, V.: Multi-site multivariate downscaling of global climate model outputs: an integrated framework combining quantile mapping, stochastic weather generator and Empirical Copula approaches, Clim. Dyn., 52, 5775–5799, https://doi.org/10.1007/s00382-018-4480-0, 2019.

Liu, Y., Xu, Y., Zhang, F., and Shu, W.: A preliminary study on the influence of Beijing urban spatial morphology on near-surface wind speed, Urban Clim., 34, 100703, https://doi.org/10.1016/j.uclim.2020.100703, 2020.

MacMartin, D. G. and Kravitz, B.: Dynamic climate emulators for solar geoengineering, Atmos. Chem. Phys., 16, 15789–15799, https://doi.org/10.5194/acp-16-15789-2016, 2016.

McSweeney, C. F. and Jones, R. G.: How representative is the spread of climate projections from the 5 CMIP5 GCMs used in ISI-MIP?, Clim. Services, 1, 24–29, https://doi.org/10.1016/j.cliser.2016.02.001, 2016.

Meng, X. G., Guo, J. J., and Han, Y. Q.: Preliminarily assessment of ERA5 reanalysis data, J. Mar. Meteor., 38, 91–99, https://doi.org/10.19513/j.cnki.issn2096-3599.2018.01.011, 2018, in Chinese.

Michalakes, J., Chen, S., Dudhia, J., Hart, L., Klemp, J., Middlecoff, J., and Skamarock, W.: Development of a next-generation regional weather research and forecast model, Developments in Teracomputing, edited by: Zwieflhafer, W. and Kreitz, N., World Scientific, 269–296, https://doi.org/10.1142/9789812799685_0024, 2001.

Moore, J. C., Yue, C., Zhao, L., Guo, X., Watanabe, S., and Ji, D.: Greenland ice sheet response to stratospheric aerosol injection geoengineering, Earth's Future, 7, 1451–1463, https://doi.org/10.1029/2019EF001393, 2019.

Ngan, F., Kim, H., Lee, P., Al-Wali, K., and Dornblaser, B.: A study of nocturnal surface wind speed overprediction by the WRF-ARW model in southeastern Texas, J. Appl. Meteor., 52, 2638–2653, https://doi.org/10.1175/JAMC-D-13-060.1, 2013.

Niemeier, U. and Timmreck, C.: What is the limit of climate engineering by stratospheric injection of SO_2?, Atmos. Chem. Phys., 15, 9129–9141, https://doi.org/10.5194/acp-15-9129-2015, 2015.

Noh, Y., Cheon, W. G., Hong, S. Y., and Raasch, S.: Improvement of the K-profile model for the planetary boundary layer based on large eddy simulation data, Bound.-Lay. Meteorology, 107, 401–427, https://doi.org/10.1023/A:1022146015946, 2003.

Pachauri, R. K., Allen, M. R., Barros, V. R., Broome, J., Cramer, W., Christ, R., Church, J. A., Clarke, L., Dahe, Q., Dasgupta, P., Dubash, N. K., Edenhofer, O., Elgizouli, I., Field, C. B., Forster, P., Friedlingstein, P., Fuglestvedt, J., Gomez-Echeverri, L., Hallegatte, S., Hegerl, G., Howden, M., Jiang, K., Jimenez Cisneroz, B., Kattsov, V., Lee, H., Mach, K. J., Marotzke, J., Mastrandrea, M. D., Meyer, L., Minx, J., Mulugetta, Y., O'Brien, K., Oppenheimer, M., Pereira, J. J., Pichs-Madruga, R., Plattner, G. K., Pörtner, H. O., Power, S. B., Preston, B., Ravindranath, N. H., Reisinger, A., Riahi, K., Rusticucci, M., Scholes, R., Seyboth, K., Sokona, Y., Stavins, R., Stocker, T. F., Tschakert, P., van Vuuren, D., and van Ypserle, J. P.: Climate Change 2014: Synthesis Report, Contribution of Working Groups I, II and III to the Fifth Assessment Report of the Intergovernmental Panel on Climate Change, edited by: Pachauri, R. and Meyer, L., Geneva, Switzerland, IPCC, p. 151, ISBN 978-92-9169-143-2, 2014.

Paulson, C. A.: The mathematical representation of wind speed and temperature profiles in the unstable atmospheric surface layer, J. Appl. Meteorol., 9, 857–861, https://doi.org/10.1175/1520-0450(1970)009<0857:TMROWS>2.0.CO;2, 1970.

Pielke Sr, R. A.: Climate vulnerability: understanding and addressing threats to essential resources, Elsevier, 2013.

Riahi, K., Rao, S., Krey, V., Cho, C., Chirkov, V., Fischer, G., Kindermann, G., Nakicenovic, N., and Rafaj, P.: RCP 8.5 – A scenario of comparatively high greenhouse gas emissions, Clim. Chang., 109, 33–57, https://doi.org/10.1007/s10584-011-0149-y, 2011.

Robock, A., Marquardt, A., Kravitz, B., and Stenchikov, G.: Benefits, risks, and costs of stratospheric geoengineering, Geophys. Res. Lett., 36, L19703, https://doi.org/10.1029/2009GL039209, 2009.

Salvi, K., Kannan, S., and Ghosh, S.: Statistical downscaling and bias-correction for projections of Indian rainfall and temperature in climate change studies, In 4th International Conference on Environmental and Computer Science, 19, 16–18 pp., IACSIT Press, Singapore, 2011.

Schmidt, H., Alterskjær, K., Bou Karam, D., Boucher, O., Jones, A., Kristjánsson, J. E., Niemeier, U., Schulz, M., Aaheim, A., Benduhn, F., Lawrence, M., and Timmreck, C.: Solar irradiance reduction to counteract radiative forcing from a quadrupling of CO_2: climate responses simulated by four earth system models, Earth Syst. Dynam., 3, 63–78, https://doi.org/10.5194/esd-3-63-2012, 2012.

Schoof, J. T., Pryor, S. C., and Ford, T. W.: Projected changes in united states regional extreme heat days derived from bivariate quantile mapping of cmip5 simulations, J. Geophys. Res.-Atmos., 124, 5214–5232, https://doi.org/10.1029/2018JD029599, 2019.

Shepherd, J.: Geoengineering the climate: Science, governance, and uncertainty, Royal Society Policy document 10/09, 82 pp., 2009.

Taylor K. E.: Summarizing multiple aspects of model performance in a single diagram, J. Geophys. Res.-Atmos., 106, 7183–7192, 2001.

Thomson, A. M., Calvin, K. V., Smith, S. J., Kyle, G. P., Volke, A., Patel, P., Delgado-Arias, S., Bond-Lamberty, B., Wise, M. A., Clarke, L. E., and Edmonds, J. A.: RCP4.5: a pathway for stabilization of radiative forcing by 2100, Climatic Change, 109, 77, https://doi.org/10.1007/s10584-011-0151-4, 2011.

Tilmes, S., Fasullo, J., Lamarque, J. F., Marsh, D. R., Mills, M., Alterskjaer, K., Muri, H., Kristjánsson, J. E., Boucher, O., Schulz, M., Cole, J. N. S., Curry, C. L., Jones, A., Haywood, J., Irvine, P. J., Ji, D., Moore, J. C., Karam, D. B., Kravitz, B., Rasch, P. J., Singh, B., Yoon, J. H., Niemeier, U., Schmidt, H., Robock, A., Yang, S. and Watanabe, S.: The hydrological impact of geoengineering in the Geoengineering Model Intercomparison Project (GeoMIP), J. Geophys. Res.-Atmos., 118, 11036–11058, https://doi.org/10.1002/jgrd.50868, 2013.

Vandyck, T., Keramidas, K., Saveyn, B., Kitous, A., and Vrontisi, Z.: A global stocktake of the Paris pledges: implications for energy systems and economy, Global Environmental Change, 41, 46–63, https://doi.org/10.1016/j.gloenvcha.2016.08.006, 2016.

Wang, J., Feng, J., Yan, Z., Hu, Y., and Jia, G.: Nested high-resolution modeling of the impact of urbanization on regional climate in three vast urban agglomerations in China, J. Geophys. Res.-Atmos., 117, D21103, https://doi.org/10.1029/2012JD018226, 2012.

Watanabe, S., Hajima, T., Sudo, K., Nagashima, T., Takemura, T., Okajima, H., Nozawa, T., Kawase, H., Abe, M., Yokohata, T., Ise, T., Sato, H., Kato, E., Takata, K., Emori, S., and Kawamiya, M.: MIROC-ESM 2010: model description and basic results of CMIP5-20c3m experiments, Geosci. Model Dev., 4, 845–872, https://doi.org/10.5194/gmd-4-845-2011, 2011.

WCRP: Coupled Model Intercomparison Project (Phase 6), CMIP6, LLNL [data set], https://esgf-node.llnl.gov/projects/cmip6, last access: 14 July 2021.

Wilby, R. L. and Dawson, C. W.: Using SDSM version 3.1 – A decision support tool for the assessment of regional climate change impacts, User manual, 8, 2004.

Wilcke, R. A. I., Mendlik, T., and Gobiet, A.: Multi-variable error correction of regional climate models, Clim. Chang., 120, 871–887, https://doi.org/10.1007/s10584-013-0845-x, 2013.

Xu, Z. and Yang, Z. L.: An improved dynamical downscaling method with GCM bias corrections and its validation with 30 years of climate simulations, J. Clim., 25, 6271–6286, https://doi.org/10.1175/JCLI-D-12-00005.1, 2012.

Yang, P., Ren, G., and Hou, W.: Temporal–spatial patterns of relative humidity and the urban dryness island effect in Beijing City, J. Appl. Meteorol., 56, 2221–2237, https://doi.org/10.1175/JAMC-D-16-0338.1, 2017.

Yu, J., Zhou, T., Jiang, Z., and Zou, L.: Evaluation of Near-surface Wind Speed Changes during 1979 to 2011 over China Based on Five Reanalysis Datasets, Atmosphere, 10, 804, https://doi.org/10.3390/atmos10120804, 2019.

Zha, J., Wu, J., Zhao, D., and Fan, W.: Future projections of the near-surface wind speed over eastern China based on CMIP5 datasets, Clim. Dynam., 54, 2361–2385, 2020.

Zhang, G., Azorin-Molina, C., Wang, X., Chen, D., McVicar, T., Guijarro, J., Chappell, A., Deng, K., Minola, L., Kong, F., Wang, S., and Shi, P.: Rapid urbanization induced daily max-

imum wind speed decline in metropolitan areas: A case study in the Yangtze River Delta (China), Urban Climate, 43, 101147, https://doi.org/10.1016/j.uclim.2022.101147, 2022.

Zhang, J., Zhao, T., Li, Z., Li, C., Li, Z., Ying, K., Shi, C., Jiang, L., and Zhang, W.: Evaluation of Surface Relative Humidity in China from the CRA-40 and Current Reanalyses, Adv. Atmos. Sci., 38, 1958–1976, 2021.

Zhao, T., Bennett, J. C., Wang, Q. J., Schepen, A., Wood, A. W., Robertson, D. E., and Ramos, M. H.: How suitable is quantile mapping for postprocessing GCM precipitation forecasts?, J. Clim., 30, 3185–3196, https://doi.org/10.1175/JCLI-D-16-0652.1, 2017.